DENTAL MATERIALS 35 (2019) 1130–1145

Available online at www.sciencedirect.com

ScienceDirect

journal homepage: www.intl.elsevierhealth.com/journals/dema

Crack-healing during two-stage crystallization of biomedical lithium (di)silicate glass-ceramics

Renan Belli[a,*], *Ulrich Lohbauer*[a], *Friedlinde Goetz-Neunhoeffer*[b], *Katrin Hurle*[b]

[a] *Friedrich-Alexander-Universität Erlangen-Nürnberg (FAU), Zahnklinik 1 – Zahnerhaltung und Parodontologie, Forschungslabor für dentale Biomaterialien, Glueckstrasse 11, 91054 Erlangen, Germany*

[b] *Friedrich-Alexander-Universität Erlangen-Nürnberg (FAU), GeoZentrum Nordbayern, Mineralogy, Schlossgarten 5a, 91054 Erlangen, Germany*

ARTICLE INFO

Article history:
Received 25 February 2019
Received in revised form
3 April 2019
Accepted 7 May 2019

Keywords:
Lithium silicate
Lithium disilicate
X-ray diffraction
Glass-ceramic
Dental
Fracture toughness

ABSTRACT

Objective. The study is aimed to evaluate the two single commercially available two-step lithium-(di)silicate systems by analyzing their parent glass composition and studying the quantitative crystalline and glass phase evolution during the second stage heat-treatment. The mechanical repercussions of the crystallization firing were evaluated using strength and fracture toughness tests.

Methods. XRF and ICP-OES were used to determine the oxide composition of the parent glasses in Suprinity PC (Vita Zahnfabrik) and IPS e.max CAD (Ivoclar-Vivadent). The crystalline phase of both materials was determined by quantitative XRD and the G-factor method in the partially and post-crystallization states. The oxide composition of the residual glass phase was derived by subtracting the chemistry of the crystalline phase fractions from the parent glass composition. Mechanical testing of biaxial flexural strength and fracture toughness were used to demonstrate how crack-like defects behave during crystallization.

Results. The two tested lithium (di)silicate systems showed strong differences in oxide composition of the parent glass. This showed to influence the transformation of lithium metasilicate in lithium disilicate, with the former remaining in high vol.% fraction in the post-crystallization Suprinity PC. In IPS e.max CAD cristobalite precipitated at the surface during the second-heat treatment. Strength and fracture toughness tests revealed that crack in both materials, whether introduced by grinding or indentation, heal during the crystallization firing. Cristobalite seemed to have contributed to a surface strengthening effect in IPS e.max CAD.

Significance. Accurate crystalline phase quantification aids in the determination of the residual glass composition in dental glass-ceramics. For both systems crystallization firing induced healing of cracks generated by CAM grinding.

* *Corresponding author at*: Laboratory for Dental Biomaterials Dental Clinic 1 – Operative Dentistry and Periodontology, Glueckstrasse 11, D-91054 Erlangen, Germany.
E-mail address: rbelli@dent.uni-erlangen.de (R. Belli).

https://doi.org/10.1016/j.dental.2019.05.013
0109-5641/

1. Introduction

Over the last thirty years, a change in the archetypal routine of glass-ceramic production in dental medicine permanently affected all levels across the processing chain of prosthetic constructs. Originally consisted of a slurry sintering protocol of leucite-reinforced glassy powders used to additively veneer metallic (and later polycrystalline ceramic) frameworks, this procedure has seen progressive discontinuation. Currently, dental glass-ceramics are supplied no longer "raw", but rather as dense, fully-sintered articles (usually standardized in cuboid block geometries) to be subtractively processed by computer aided manufacturing (CAM) technology through an intermediary service provider (dental laboratory), or directly chairside at the dentist's office.

That concept has two strategic branches: low-crystal fraction one-step materials that are ready to install after machining and polishing; or two-step materials that are machined in a partially-crystallized state and subsequently heat-treated to their end-crystallized form. On the one hand, machining of softer materials in the glassy state has the practical appeal of being faster and prolonging the lifetime of machining tools, but suffers from the inherent inconvenience of requiring a time-consuming crystallization firing. *Vice-versa*, fully-sintered ready-to-use materials allure by abdicating the need for furnace equipment (thus bypassing potential safety hazards), saving time on firing procedures, to ultimately favor the chairside course. For mechanical benefit, materials that undergo a two-stage crystallization process are designed to acquire higher crystalline content during final heat-treatment, a typical obstacle to the machinability of one-step systems. The latter are usually low-strength low-toughness, highly glassy materials indicated for reduced stress applications only.

Most of the marketed glass-ceramic products for CAM process today are of the one-step sort. Only two commercial products represent the share for two-step glass-ceramics: one is the established multi-component lithium disilicate glass ceramic developed by Ivoclar-Vivadent AG, available since 2004 and extensively described in scientific reports; the other is a product of similar composition, a glass-ceramic of the system SiO_2-Li_2O–Al_2O_3–K_2O–P_2O_5–ZrO_2, advertised as a *zirconia-reinforced lithium silicate*, developed by the Fraunhofer Institute for Silicate Research, Germany, in cooperation with DeguDent GmbH and Vita Zahnfabrik H. Rauter GmbH & Co. KG, launched in 2013. The latter material is supplied as two-step CAM-block by Vita Zahnfabrik and as one-step CAM-block by Dentsply-Sirona Inc. At stake is a multimillion-worth market of prosthetic solutions indicated for partial- and single-unit reconstructions onto natural teeth and implant abutments. De facto, a clinical trend of two-step materials being preferred over the conventional one-step approach is ongoing [1].

Remarkably, despite being classified as medical products available over-the-counter, little information regarding their composition is known apart from what companies describe in their product brochures and data-sheets. The oxide formulation of the parent base glass is given in a wide range of wt.%, with the volume fraction of the crystalline and glass phases expressed as rough estimations. This represents a serious barrier to a deeper understanding of the mechanical behavior of such materials, limiting its applicability for use in clinical lifetime predictions. One important mechanical aspect that concerns glass-ceramic materials is the damage sustained during machining with coarse diamond tools that follows from a typical dental CAM process. Experimentally, grinding low-crystal fraction dental glass-ceramics has been shown to produce subsurface cracks that lead to significant strength degradation [2,3]. This is a known effect in brittle materials [4,5]. In leucite- and feldspar-based one-step glass-ceramics, annealing seems to be ineffective in strength recovery from grinding damage [3,6]. In two-step systems, grinding damage has been accounted for premature fractures of CAM-processed partially-sintered zirconia-based prostheses clinically [7], confirming experimental observations that cracks are not healed during sintering of 3Y-TZP to full density [8,9]. In two-step lithium silicate materials, the fate of machining cracks induced in the pre-crystallization state that undergo a secondary crystallization firing has yet to be described.

Here we provide a thorough characterization of the two above mentioned two-step lithium silicate materials by describing the evolution of the crystalline and the glassy phase during the two-stage crystallization process. The effects of crystallization firing on the healing of cracks induced by grinding and indentation is addressed in extensive strength and fracture toughness testing and illustrated using fundamental fracture mechanics relations.

2. Materials and methods

2.1. Materials

Currently two lithium-based silicate glass-ceramics are commercially available being supplied in a partially-crystallized state for machining to undergo a subsequent "crystallization firing". The first variant (IPS e.max® CAD) belongs to the third generation of the so-advertised *lithium disilicate* glass-ceramic developed by Ritzberger et al. [10] in the 90s for dental applications, commercialized by the company Ivoclar-Vivadent (Schaan, Liechtenstein). It is indicated for clinical use for partial-, single- and 3-unit reconstructions, single- or multi-unit overlays fused onto zirconium dioxide frameworks and as monolithic abutments for dental implants. Having being installed in millions of patients to the date, a recent retrospective cohort population-based study reported for this material in-service fracture rates of 0.83% after 3.5 years, with lifetime estimations of at least 21 years for reaching 10% of fractures based on a poll of about 22 thousand restorations [1]. The material is delivered as blueish-tinted blocks in the glassy-crystalline form, intended to be machined down to the shape of application following a typical CAD/CAM processing. A recent phase composition analysis revealed in this stage a main lithium metasilicate (Li_2SiO_3) phase and traces of lithium orthophosphate (Li_3PO_4), both using Raman spectroscopy and X-ray diffraction analysis [11]. A heat treatment of the machined piece follows from that, for 10 min at 850 °C, after which the material attains the desired tooth color and final physical and mechanical properties. In Ref. [11] only

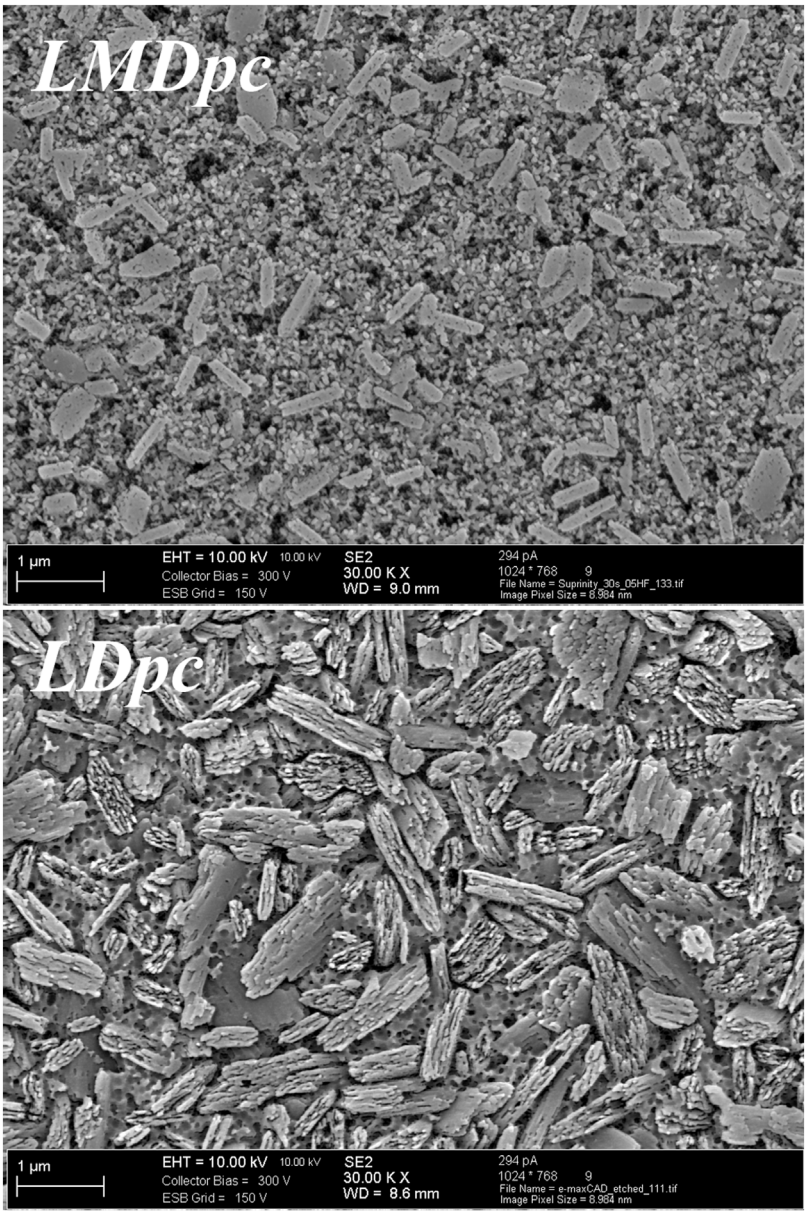

Fig. 1 – Scanning electron microscopic images of the two lithium-based silicate glass-ceramics evaluated in their post-crystallization states. *LMDpc* was etched with a 0.5% hydrofluoric acid solution for 30 s. The submicrometric crystal phase is $Li_2Si_2O_5$ and the nanometric granules are Li_2SiO_3 crystals. *LDpc* was etched with 5% hydrofluoric acid solution for 30 s. Only the $Li_2Si_2O_5$ crystal phase is visible. The Li_3PO_4 crystals in both materials were dissolved by etching.

lithium disilicate ($Li_2Si_2O_5$) and Li_3PO_4 were detected in the material following the prescribed second heat-treatment. This material will be hereafter termed *lithium disilicate* (*LD*) due to the main phases in the post-crystallization state.

The second variant (Suprinity® PC) is marketed by the company Vita Zahnfabrik (Bad Säckingen, Germany) since 2013 to compete with the well-established IPS e.max® CAD material for most of its clinical indications. It is advertised as a *zirconia-reinforced lithium silicate* due to an alleged 8–12 wt.% ZrO_2 addition to the initial glass composition. After machining, the material Suprinity® PC undergoes a heat treatment for 8 min at 840 °C. In the partially-crystallized state, it has been shown to be comprised of Li_2SiO_3 and Li_3PO_4 phases by Raman spectroscopy, both persisting in the material after crystallization firing with an additional $Li_2Si_2O_5$ phase appearing [11]. This material will therefore be hereafter termed *lithium metasilicate disilicate* (*LMD*). No crystalline ZrO_2 was found in both pre- and post-crystallization states [11]. Scanning electron micrographs of the crystallized materials after etching are illustrated in Fig. 1.

For clarity purposes, prefix as follows will be used throughout the text to refer to the: parent glass (*pg*), residual glass (*rg*), and pre-crystallization (*pc*) state of the *LMD* and *LD* materials, to form acronyms such as *pgLMD*, *pcLMD*, *rg-pcLMD*, etc. The post-crystallization form will use the suffix *pc* after the material acronym, such as *LDpc* or *rgLDpc*.

Table 1 – ICSD structures used for the refinement of crystalline phases present in *LMD* and *LD* in the pre- and post-crystallization states.

Phase	ICSD #	Space group	Authors
Li_2SiO_3	853	Orthorhombic $Cmc2_1$	Hesse [17]
$Li_2Si_2O_5$	280481	Orthorhombic Ccc2	de Jong et al. [18]
Li_3PO_4	25816	Orthorhombic Pmnb	Zemann [19]
$Y_4Al_2O_9$	63650	Monoclinic $P2_1/c$	Lehmann et al. [20]
Y_2O_3	66243	Cubic Ia-3	Smrcok and Duris [21]
Tb_2O_3	33653	Cubic $I2_13$	Zachariasen [22]
SiO_2 (Cristobalite)	75300	Tetragonal $P4_12_12$	Downs and Palmer [23]

Details about the specific composition of the precursor (parent) glass and phase quantification in the pre-crystallization and post-crystallization materials are not disclosed by the manufacturers, nor available in the scientific literature to date. In the product data sheets, as well as available patents, only wt.% ranges of the oxides constituting the parent glass composition are given, and likewise estimated crystallinity (vol.% crystal content), for example for IPS e.max® CAD as ~70 vol.%. In our preliminary analysis of Suprinity® PC, the composition of the parent glass was determined by X-ray Fluorescence Spectroscopy (XRF) and Inductively Coupled Plasma Optical Emission Spectroscopy (ICP-OES) [12]. Quantitative phase composition, namely the wt.% of the different crystalline phases and the residual glass, was determined by XRD using the G-factor method, an external standard method, allowing the estimation of the oxide composition of the residual glass in the pre-crystallization and post-crystallization states (See Table 5) [12]. Here this method is extended to determine the phase quantification of both systems, specifically at the surface of samples and at the bulk (see Section 2.2).

2.2. *Analysis of phase composition*

Samples from the same batches (Lot 56800 for *LMD*; Lot U56822 for *LD*) were used throughout this study. Blocks with dimensions of approx. $14 \times 12 \times 18\,mm^3$ were sawed along their long axis using a water-cooled diamond-embedded copper disc to obtain rectangular plates. In the preliminary measurements of material *LMD* [12], the reproducibility of the measurements in three different samples within the same block and among three different blocks was excellent. Therefore, for the material *LD* only one sample per block was evaluated, in a total of three blocks.

The quantitative phase composition of the samples was determined by XRD at a D8 diffractometer (Bruker AXS, Karlsruhe) equipped with a 9-fold sample changer. The following measurement conditions were applied: range 6°–70° 2θ; step size 0.011° 2θ; integration time 0.3 s; radiation: copper K_α; generator settings: 40 kV, 40 mA; divergence slit: variable V12; detector: LynxEye. Both materials were evaluated before and after the final heat-treatment. In order to analyze possible surface effects, which might occur during the crystallization firing, post-crystallization samples were measured before and after grinding with a fine diamond wheel (D15), used to remove ~0.5 mm in thickness. For XRD measurements, the samples were prepared into special sample holders.

The software TOPAS 4.2 (Bruker AXS, Karlsruhe) was used for Rietveld refinement. The ICSD structures used for refinement are presented in Table 1. A *hkl* phase derived from the structure of Li_2SiO_3 was created to fit the contribution of the amorphous glass phase. For *hkl* phases, no atom positions are needed, only a space group and lattice parameters. Hence, they can be applied to fit amorphous or crystalline phases lacking an available structure model. The anisotropic crystallinity of the Li_2SiO_3 and Li_3PO_4 coherent scattering domains (CSDs) was refined with a special cuboid model [13,14], where *rx* was aligned parallel to the crystallographic *a* axis, *ry* to the *b* axis and *rz* to the *c* axis for each phase [15]. The crystallite size "*True CS*", which is defined as the cube root of the volume of the geometric model [16], was then calculated according to Eq. (1):

$$True\,CS = \sqrt[3]{8 \cdot rx \cdot ry \cdot rz} \tag{1}$$

For $Li_2Si_2O_5$, the parameters isotropic crystallite size CS_L (Lorentz contribution) and microstrain Str_L (Lorentz contribution) were refined. In the not-ground *LMD* sample, preferred orientations in the (1 0 1) and the (1 1 0) direction were introduced for Li_3PO_4 to obtain a satisfactory fit.

As in Ref. [12], the absolute quantities of the crystalline phases and the amorphous content of the two glass-ceramics were obtained by application of the G-factor method, an external standard method [15]. A quartzite slice (fine grained rock of almost pure quartz), calibrated with 100% crystalline silicon powder (NIST Si Standard 640d) to obtain c_q, was used as external standard. The G-factor was determined from measurements of quartzite under identical measurement conditions as the samples according to Eq. (2) [24]:

$$G = S_q \frac{\rho_q V_q^2 \mu_q^*}{c_q} \tag{2}$$

The Rietveld scale factor of quartz (S_q), the density of quartz (ρ_q) and the unit-cell volume of quartz (V_q) were obtained from Rietveld refinement of the quartz in quartzite. The mass attenuation coefficient (mac) of quartz ($\mu_q{}^*$) was calculated from the macs of the constituting elements, which were taken from the International Tables for Crystallography [25].

The absolute quantity of any crystalline phase *j* present in the samples can then be determined from the Rietveld scale factors using Eq. (3):

$$c_j = S_j \frac{\rho_j V_j^2 \mu^*_{sample}}{G} \tag{3}$$

The difference of the sum of all quantified crystalline phases to 100 wt.% is then the amorphous content, which might also include undefined phases or remaining misfits

Table 2 – Mass fraction in wt.% of the crystalline and glass phases in the *LMD* and *LD* materials in the pre-crystallization and post-crystallization states. The phase fractions in vol.% for the post-crystallization bulk samples are given in brackets.

		Li_2SiO_3	$Li_2Si_2O_5$	Li_3PO_4	Y_2O_3	Tb_2O_3	$(Y,REE)_4Al_2O_9$	Cristobalite	Amorphous (glass)
LMD	Pre-crystallization	41.9 ± 2.3 [42.7 vol.%]	–	–	–	–	–	–	58.1. ± 2.3 [57.3 vol.%]
	Post-crystallization bulk	25.6 ± 0.4 [27.1 vol.%]	13.3 ± 0.7 [14.4 vol.%]	10.7 ± 0.3 [11.6 vol.%]	–	–	0.17 ± 0.13	–	50.1 ± 1.0 [53.0 vol.%]
	Post-crystallization surface	24.2 ± 0.3	17.4 ± 0.4	10.7 ± 0.3	0.7 ± 0.1	1.5 ± 0.3	–	–	45.9 ± 0.8
LD	Pre-crystallization	34.0 ± 0.2 [32.6 vol.%]	0.7 ± 0.1 [0.7 vol.%]	4.0 ± 2.0 [3.9 vol.%]	–	–	–	–	62.0 ± 2.0 [62.7 vol.%]
	Post-crystallization bulk	–	59.7 ± 0.5 [60.3 vol.%]	6.8 ± 0.4 [6.9 vol.%]	–	–	–	–	33.5 ± 0.9 [32.9 vol.%]
	Post-crystallization surface	–	59.0 ± 1.5	7.3 ± 0.9	–	–	–	1.0 ± 0.4	32.7 ± 1.9

from the refinement of the crystalline phases. The chemical compositions of the parent glasses for both *LD* and *LMD* were obtained by XRF and the lithium fraction by ICP-OES. These were used for calculation of the μ^*_{sample} for both compositions.

The chemical composition of both glass-ceramic blocks, which should match the oxide composition of the parent glass used by the manufacturer, was determined by XRF. Additionally, lithium was measured by ICP-OES. For preparation, the blocks were grinded by a disc mill with a tungsten carbide milling set. From this powder, a fusion tablet was fabricated with addition of $Li_2B_4O_7$ for XRF; this was performed with a wavelength dispersive X-ray spectrometer from Bruker AXS. Fusion casting was performed for ICP-OES analysis (720-ES, Varian) with axial plasma observation and an Echelle spectrometer with cooled CCD detector was used. Maximum overall measurement uncertainty was 10% for XRF and 6.6% for ICP-OES (Li).

The oxide composition of the residual glass phase before and after crystallization firing was calculated by combining the quantitative XRD data with the parent glass chemistry obtained from XRF and ICP-OES. For each mineral phase quantified with the G-factor method, the normative content of the constituting oxide in this phase was multiplied with the quantity of the corresponding crystalline phase in the sample. The results were then subtracted from the content of the corresponding oxide in the sample. The remaining percentages of the oxides were then normalized to 100 wt.%. The phase fraction in vol.% was determined by calculating the volume that would be present in 1 g of glass ceramic for each crystalline phase from the wt.% obtained by XRD and the density of the corresponding phase. Accordingly, the volume of 1 g of glass-ceramic was determined via the density of the whole glass-ceramic measured for *LMDpc* and *LDpc* in Ref. [11] obtained by Resonant Ultrasound Spectroscopy (RUS). The density of *pcLMD* was obtained from Ref. [26], while the density of *pcLD* was estimated to be slightly below that of *LDpc*. The volume fraction of each crystalline phase could then be easily obtained by dividing the volume of the corresponding phase by the volume of the whole glass-ceramic.

2.3. *Strength testing*

Blocks of the two pre-crystallized systems, as received from the manufacturers, with dimensions of approx. $14 \times 12 \times 18\,mm^3$ were ground with a fine diamond wheel (D46) to obtain square cross-sections of $12 \times 12\,mm^2$ for the later sectioning of plate-shaped specimens. Seven slices with thickness of 1.50 mm were cut from each block using a diamond-coated copper disc mounted to a precision cutting machine (IsoMet 5000, Buehler, Illinois, USA) under water irrigation. Over thirty specimens were produced per material for each of the following five experimental groups: (i) pre-crystallized specimens were ground and not further treated; (ii) pre-crystallized specimens were ground, subsequently crystallized and no further treated; (iii) pre-crystallized specimens were crystallized and subsequently ground; (iv) pre-crystallized specimens were polished, subsequently crystallized and no further treated; (v) pre-crystallized specimens were crystallized, subsequently polished and no further treated. All grinding procedures for the specimens

Table 3 – Refined values for anisotropic crystallite sizes of the phases present in pre- and post-crystallization samples of the *LMD* material.

Crystal	CSDs	Pre-crystallization	Post-crystallization	
			Surface	Bulk
Li_2SiO_3	rx [nm]	1.42 ± 0.15	21.1 ± 1.5	17.4 ± 0.9
	ry [nm]	5.28 ± 0.54	28.4 ± 1.1	25.4 ± 1.4
	rz [nm]	1.19 ± 0.08	37.7 ± 1.6	28.2 ± 1.4
	True CS [nm]	4.2 ± 0.4	57 ± 3	46.4 ± 2.4
$Li_2Si_2O_5$	Strain_L	–	0.30 ± 0.01	0.20 ± 0.01
	CS_L [nm]	–	–	229 ± 15
Li_3PO_4	rx [nm]	–	26 ± 13	8.4 ± 1.2
	ry [nm]	–	5 ± 1	4.7 ± 0.3
	rz [nm]	–	10 ± 1	6.4 ± 0.7
	True CS [nm]	–	21 ± 3	12.7 ± 1.3

Table 4 – Refined values for anisotropic crystallite sizes of the phases present in pre- and post-crystallization samples of the *LD* material.

Crystal	CSDs	Pre-crystallization	Post-crystallization	
			Surface	Bulk
Li_2SiO_3	rx [nm]	14.5 ± 0.7	–	–
	ry [nm]	10.1 ± 0.1	–	–
	rz [nm]	14.7 ± 0.2	–	–
	True CS [nm]	25.8 ± 0.4	–	–
$Li_2Si_2O_5$	Strain_L	–	0.22 ± 0.01	0.22 ± 0.01
	CS_L [nm]	–	–	–
Li_3PO_4	rx [nm]	3.4 ± 0.6	5.1 ± 0.2	6.0 ± 0.4
	ry [nm]	4.5 ± 1.6	10.2 ± 2.8	8.2 ± 0.6
	rz [nm]	3.4 ± 0.6	2.7 ± 0.2	3.3 ± 0.3
	True CS [nm]	7.4 ± 1.8	10.4 ± 1.4	11.0 ± 0.7

Table 5 – Composition of the glass phase of the *LMD* and *LD* materials in [wt.%] in the pre-crystallization and post-crystallization states.

Oxide	Parent glass[a]		Pre-crystallization[b]		Post-crystallization[b]	
	LMD	*LD*	*LMD*	*LD*	*LMD*	*LD*
Glass phase	100	100	58.1 ± 2.3	62.0 ± 2.0	50.1 ± 1.0	33.5 ± 0.9
SiO_2	57.5	71.9	51.0	79	58.4	67
Al_2O_3	2.02	3.51	3.5	5.7	3.9	9.7
TiO_2	<0.01	0.01	–	–	–	–
Fe_2O_3	0.05	0.05	0.1	0.06	0.1	0.14
CaO	0.04	0.04	0.1	0.06	0.1	0.1
K_2O	1.89	4.00	3.2	6.5	3.7	11
MgO	0.15	0.17	0.3	0.28	0.3	0.47
Na_2O	0.03	0.06	0.1	0.10	0.1	0.17
CeO_2	1.96	2.50	3.4	4.1	3.8	6.9
Li_2O	18.3	12.7	7.5[d]	0(-0.28)	5.8	0 (−1.8)
Cr_2O_3	<0.01	<0.01	–	–	–	–
P_2O_5	5.75	3.30	9.9[d]	1.4	0 (−0.75)	0 (−0.87)
Tb_4O_7	1.54	0.51	2.6	0.83	3.0	1.4
Er_2O_3	0	0.29	–	0.47	–	0.80
HfO_2	0.24	–	0.4	–	0.5	–
V_2O_5	0.16	0.13	0.3	0.21	0.3	0.36
Y_2O_3	0.61	–	1.0	–	0.8	–
ZrO_2	9.78	0.81	16.8	1.3	19.2	2.2
Sum	99.91	99.90	100.20	100.01	100.00	100.24
Lost[c]	0.09	0.1	–	–	–	–

[a] Obtained using XRF and ICP-OES.
[b] Calculated based on XRD and G-factor method.
[c] Relative amount of lost oxide during melting and casting, determined at 1050 °C.
[d] The relative amount of P_2O_5 and Li_2O in the residual glass of *pcLMD* material was estimated based on the absence of Li_3PO_4 peaks related to the disordered structure of Li_3PO_4 in this stage.

with grinding-finish at the surface were undertaken as follows: the specimens were fixed to a metallic blank with perfect parallel sides using a thermoplastic resin and ground under water irrigation using a diamond wheel of 8 mm rim width and D91 diamond gain size embedded in a copper matrix. Specimens were ground down to 1.20 ± 0.05 mm (see Fig. 1a). For the specimens with a polished surface finish, an 8 mm-width rim wheel with D15 diamond grain size embedded in a resin matrix was used to reduce the thickness down to ~1.25 mm. The final specimen thickness of 1.20 ± 0.05 mm was achieved by polishing procedures using decreasing SiC papers (P600, P800, P1200, P2500 and finally P4000) under water irrigation in an automatic polishing machine under 40 N force. Specimens were debonded from the resin by heating up to ~100 °C, slowly cooled to room temperature and thoroughly cleaned with acetone.

The parameters for the crystallization firing corresponded to those in the manufacturer's instructions. The *LMD* material underwent a crystallization firing for 8 min at 840 °C (heating rate 55 °C/min), while the *LD* material underwent a crystallization firing for 10 min at 850 °C (heating rate 30 °C/min). The specimens were positioned inside the oven (Vacumat 4000, Vita Zahnfabrik) on top of a fibrous alumina pad that allowed homogeneous heat distribution through the thickness. During the cooling phase, the furnace was kept closed until 680 °C was reached; after that the chamber's lift opened down to expose the specimens to convective air (~22 °C). Roughness measurements of 10 random specimens per group were performed with a high resolution confocal optical profilometer (CT 100, CyberTechnologies, Germany) over a 1 mm^2 area at the center of the specimen with x–y step-sizes of 1 μm and a vertical resolution of 0.02 μm.

The ball-on-three-balls (B3B) biaxial strength test, first introduced by Börger et al. [27], was conducted using an especially designed assembly. The well-defined load transfer in the B3B (three-point contact) allows testing of specimens with flatness deviations up to 16% [28], and small warpings present in as-sintered specimens. The influence of friction is considerably reduced when compared to fixed supports, as the loading balls roll outward during bending of the specimen [28]. Unlike rotationally symmetric set-ups (e.g., ring-on-ring), the stress field at the tensile side of the specimen has a threefold symmetry in the B3B assembly [27]. The load is transferred through a small contact area to the specimen by the central ball, with generated tensile stresses being highly dependent upon the radius of this contact area, which is, in turn, a function of the elastic moduli of the tested material and balls [27]. The thickness of the B3B specimens was measured at their center with rounded-tip digital dial gages with resolution of +/−0.002 mm (ID-C112XB, Mitutoyo, Japan). Support and loading balls with the same radius (R_b = 4 mm) were used. Specimens were tested in a universal testing machine (Z2.5, ZwickRoell, Ulm, Germany) at a cross-head speed of 1.5 mm/min to minimize slow crack growth (fracture took place within 5–10 s). In the used B3B assembly device (see Fig. 2b, c and Ref. [29] for details), the treated surface is placed facing up and is the surface supporting the three loading balls. The biaxial strength was calculated using Eq. (4), as the maximum principal stress that takes place at the center top of the specimen, which scales with the force applied F, and the inverse of the square root of the thickness t:

$$\sigma_{max} = \delta \frac{F}{t^2} \tag{4}$$

where δ is a function derived using finite element analysis for the specific assembly and specimen geometry used in this study [29], and reads:

$$\delta = f\left(\frac{t}{R_a}, \nu\right) = 0.323308 + \frac{(1.30843 + 1.44301\nu) \times \left[1.78428 - 3.15347\,(t/R_a) + 6.67919(t/R_a)^2 - 4.62603(t/R_a)^3\right]}{1 + 1.71955\,(t/R_a)} \tag{5}$$

where ν is the Poisson's ratio of the tested material, taken from Ref. [11]. As the Poisson's ratios for the pre-crystallized materials were not known, ν of the fully-crystallized samples were used in both occasions as a reasonable approximation. By using rectangular plates instead of discs as specimens, the test loses the three-fold symmetry and acquires a mirror-symmetry that intersects one of the loading points. Because the extra material on the edges of plates stiffens the specimen, an important effect on the bending strain is observed, requiring a special numerical analysis for the function δ. Strength values obtained using the B3B test with rectangular plates have been validated extensively for alumina, silicon nitride and a capacitor ceramic in Refs. [30] and [31]. Rectangular plate testing has been shown to yield values comparable to those obtained with discs described by the prediction of Weibull scaling theory [29].

2.4. *Fracture toughness (K_{Ic}) testing*

A better insight into a potential healing effect of cracks created in the two lithium silicate systems as consequence of grinding can be obtained by calculating the size of the critical cracks inducing failure in the strength experiments. For that, the Irwin-Griffith relationship between fracture strength and critical crack size at instability, a_c, comes in handy:

$$K_{Ic} = \sigma_{max} Y \sqrt{\pi a_c}\,, \tag{6}$$

provided that the stress intensity factor in mode I loading, K_{Ic} (or the fracture toughness), is known for the pre-crystallization materials. This allows for a comparison of the magnitude of the grinding damage also in the post-crystallization state by employing the K_{Ic}-values of the material after the crystallization firing in Eq. (3). Those have been measured for both systems using the B3B-K_{Ic} method in Refs. [32,33] (see Table 8). The B3B-K_{Ic} test is a modification of the surface-crack-in-flexure method standardized in ASTM C1421 [34] for beams loaded in uniaxial 4-point bending. For consistency with the results in Refs. [32,33], the B3B-K_{Ic} method was selected for the measurement of the fracture toughness under two conditions: (i) the surface pre-cracks were produced in the pre-crystallized materials without fur-

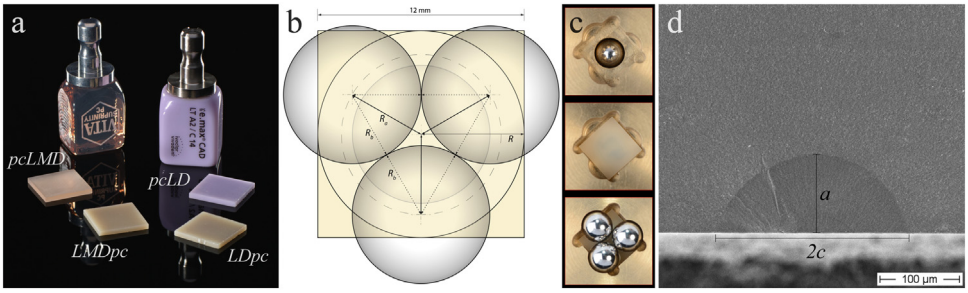

Fig. 2 – (a) Plate specimen geometry for B3B strength and B3B-K_{Ic} testing prepared from pre-casted blocks of the *LMD* and *LD* materials, in the pre-crystallization and post-crystallization stages. (b) Detailed schematic of the geometry of the B3B set-up. In (c) the specimens are placed in the assembly with the treated or indented surface faced upwards, where the maximum tensile stress is generated during testing. (d) SEM image of an artificially created semi-elliptical shaped pre-crack using Knoop indentation and polishing, used for K_{Ic} determination; crack dimensions *a* and *2c* are measured on the fracture surfaces.

ther treatment and; (ii) the surface pre-cracks were produced in the pre-crystallized materials, which subsequently underwent the respective crystallization firing.

Pre-cracks were produced by Knoop indentation of polished surfaces nearest to the location right above the loading ball, determined previously in a light microscope; the direction of the indentation's long axis was marked on the specimen so to properly orient it during positioning in relation to the supporting balls. Specimens were tilted in 0.5° to facilitate posterior fractographic identification of the pre-cracks. Indentation loads of 2.5 kg and 3 kg were used for *pcLD* and *pcLMD*, respectively, so to produce a critical flaw size of comparable dimensions to those produced in Refs. [32,33] for the post-crystallization materials, this way avoiding any potential crack-size effect. The full load dwell time consisted of 15 s. The removal of the damage zone produced by the indenter was accomplished using dry P600 SiC paper and constant evaluation of the indented surface under 200× magnification until the lateral cracks were completely removed. Here the specimens to be crystallized underwent the firing schedules as previously described.

Prior to testing, the specimens were dried in an oven at 150 °C for 2 h and immediately immersed in silicon oil (also dried at 150 °C for 2 h), in order to minimize the occurrence of water-assisted subcritical crack growth during loading. The fracture toughness was calculated using the maximum force F_{max} at fracture and the solution [35,36]:

$$K_{Ic} = \sigma_{max} \times Y_{B3B} \times \sqrt{\pi a} = \left(\frac{F_{max}}{t^2} \times \delta\right) \times Y\left(\frac{a}{c}, \frac{a}{t}, \frac{t}{R_a}, \nu\right) \times \sqrt{\pi a} \quad (7)$$

where *t* is the thickness of the specimen, the support radius is formed by the three supporting balls in contact $R_a = 2\sqrt{3} \times R_b/3$ (R_b = 4 mm is the radius of the supporting balls), and ν is the Poisson's ratio of the material. The Y factor for the B3B-K_{Ic} test is derived based on the simulations of Strobl et al. [37,38], having *a* (depth) and *c* (half the length at the surface) as the pre-crack dimensions. The geometry factor for surface cracks in bending, given in ASTM C 1421, is the solution by Newman and Raju [39], derived for the general case of ν = 0.3. Strobl et al. [37] refined the finite element calculations for the semi-elliptical crack geometry and provided a solution for a broader range of ν, including the range between 0.2–0.3 of most glasses and ceramics, also taking in consideration the termination angle of the semi-elliptical crack at the surface. The angle formed between the surface and a tangent touching the point the crack terminates at the surface, as well as both crack dimensions *a* and 2*c*, were measured on the SEM images of the pre-cracks after fracture (see Fig. 1d) using an image software (ImageJ).

Errors can occur during the B3B-K_{Ic} test; a dedicated analysis is found in Ref. [35]. These concern mainly: (i) the positioning of the pre-crack relative to the center of the support radius and; (ii) the orientation of the pre-crack relative to the supporting balls. From the three positioning errors that are possible in reference to the symmetry axis, namely rotation α, normal shift (out-of-plane, Δx) and tangential shift (in-plane, Δy), the latter can be assessed fractographically by determining the positions of the pre-crack and the loading point. In Ref. [32] a poll of over 70 B3B-K_{Ic} specimens revealed a trend of lower positioning errors being induced in square compared to round specimens, with a mean overestimation of 0.8–1.25% due to in-plane shift and an expected 1–4% additional error if a maximum $\Delta x = \Delta y$ occurs. We performed this analysis also for the B3B-K_{Ic} specimens of partially-crystallized specimens, with the values given in Table 8 having been corrected by 1.13%–1.92% without considering out-of-plane shift errors.

3. Results and discussion

3.1. *Crystallinity and phase evolution after crystallization firing*

In Table 2 the mass fractions of the quantified crystalline and the calculated residual glass phases are summarized for the pre- and post-crystallization materials. A good fit for the Li_2SiO_3 phase was not possible using a refinement for isotropic crystallinity in the Rietveld software. While a satisfactory fit could be obtained by introducing a preferred orientation for Li_2SiO_3 in the (0 1 0) plane, the actual presence of crystalline growth preferred in one direction was unambiguously excluded in our preliminary study [12]. Crystallite sizes (phys-

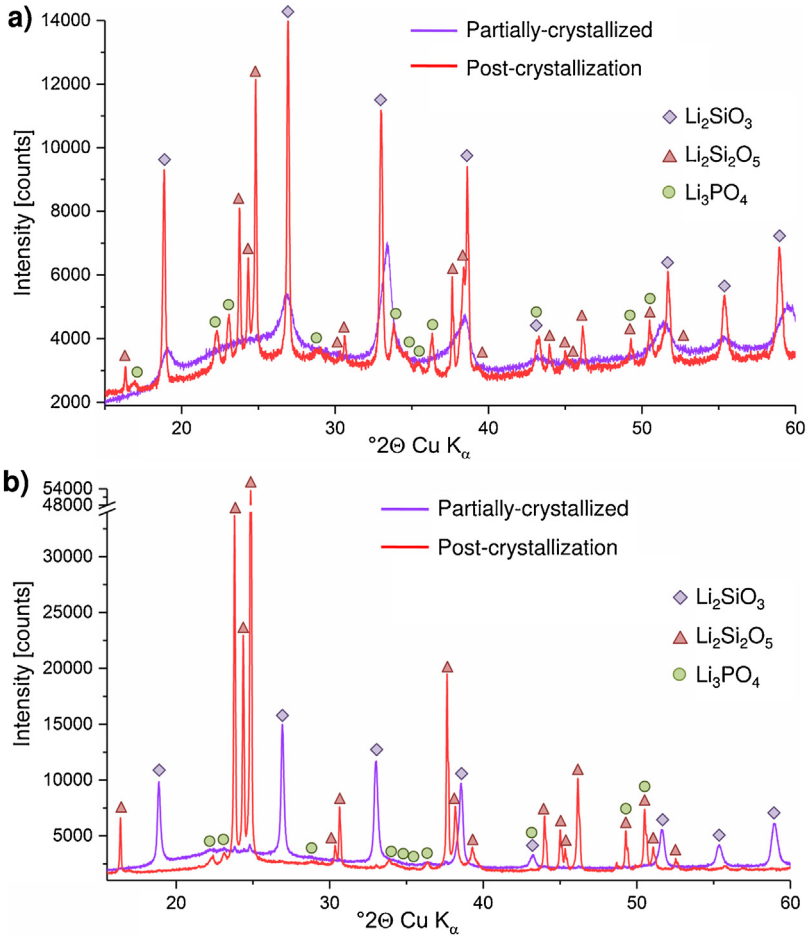

Fig. 3 – Diffraction patterns of the lithium silicate glass-ceramics (a) *LMD* and (b) *LD* before and after the crystallization firing.

ically described as coherent scattering domains, CSD) were therefore refined using an anisotropic cuboid crystallinity model [13,14], supported by the sharper (0 2 0) reflection in the diffraction patterns for the *pcLMD* (see Fig. 3).

The data obtained for the refined CSD dimensions revealed that the crystallite anisotropy of the Li_2SiO_3 phase in the *pcLMD* and *pcLD* materials is different (Tables 3 and 4). While the CSDs are elongated in the *b* axis for the former with an aspect ratio of *ry/rz* = 4.4 ± 0.2, the *b* axis is shorter compared to *a* and *c* for *pcLD* (aspect ratio *ry/rz* = 0.68), and the extent of anisotropy is lower. By taking into account the dimensions of lattice parameters *a*:*b*:*c* the number of lattice planes (number of unit cells aligned in the same direction) is 3:20:5 for the *pcLMD* material and 31:37:61 for the *pcLD* material, with a True CS of 4.2 ± 0.4 nm and 25.8 ± 0.4 nm, respectively. Hence there are rather small crystals in *pcLMD* with remarkable CSD size anisotropy present in high density if its high content (~42 wt.%) is considered. In contrast, Li_2SiO_3 crystals in *pcLD* seemed to have grown larger, but in fewer nucleation sites, and with a lower extent of CSD size anisotropy. The presence of only small fractions of $Li_2Si_2O_5$ and Li_3PO_4 in *pcLD*, while solely Li_2SiO_3 was formed in *pcLMD* as crystalline phase detectably by XRD during the first heat-treatment, hints to considerable differences in the crystallization behavior that seem to be strongly contingent on small changes in the primary oxide composition.

Of most importance in multi-component lithium (di)silicate systems are: (i) the SiO_2/Li_2O molar ratio and (ii) the amount of the nucleation agents P_2O_5 and ZrO_2. In that regard, a look at the XRF/ICP-OES results in Table 5 reveals clear differences between the two materials: *pgLMD* has about two times the amount of P_2O_5 and a ten-fold higher content of ZrO_2 compared to *pgLD*, with SiO_2/Li_2O molar ratios of 1.56 and 2.81, respectively. For compositions similar to *pgLD* [40–42], Li_2SiO_3 begins to form at around 560–580 °C, simultaneously to a very low-intensity crystallization of $Li_2Si_2O_5$, which starts to grow faster only at higher temperatures (>750 °C) following to the decomposition of the Li_2SiO_3 phase. The presence of $Li_2Si_2O_5$ phase under 1 wt.% in the *pcLD* indicates that the first heat-treatment took place somewhere below 750 °C, even though Li_3PO_4 (4 wt.% fraction) should only appear after 780 °C [42] in its mature crystallized form. The Li_3PO_4 detected in *pcLD* might in fact represent its poorly crystallized disordered structure that promotes the heterogeneous nucleation of Li_2SiO_3 at its interface with the glass matrix in systems having P_2O_5 as nucleation agent [43]. Based on the higher crystallinity exhibited by Li_2SiO_3 in *pcLD* than in *pcLMD*, one might risk to assume that these disordered Li_3PO_4 seeds might have reached sufficient dimensions

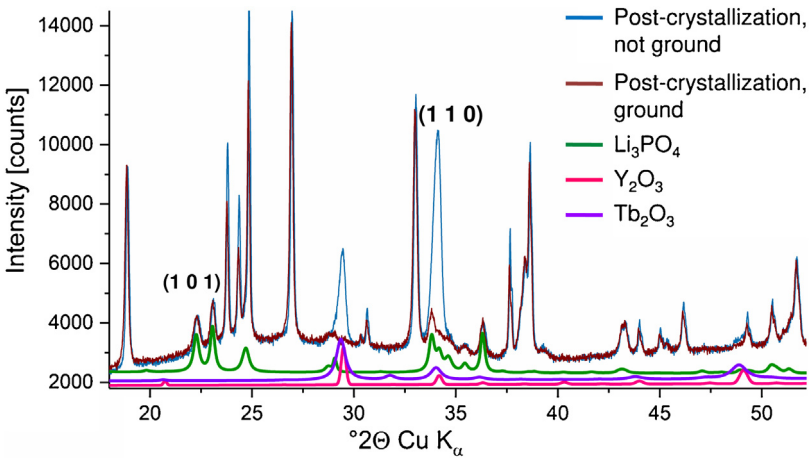

Fig. 4 – Diffraction patterns of *LMDpc* before and after grinding; the patterns of the crystalline phases were calculated with software TOPAS.

(CSD = 7.4 nm) to be detected by XRD, which is not always the case. In *pcLMD*, Li_3PO_4 was not detected by XRD, but by Raman spectroscopy in Ref. [11], and observed to appear at 647 °C, shortly before Li_2SiO_3, which was shown to form at 658 °C in experiments where *pcLMD* was melted and re-heated [26]. The higher crystallization temperature of Li_2SiO_3 in *pcLMD* might stem from the high concentration of ZrO_2 in the glass (~10 wt.%), an additive that shifts the onset of crystallization of Li_2SiO_3 toward higher temperatures [41,44,45], and inhibits the completion of $Li_2Si_2O_5$ nucleation at a temperature of 850 °C [41]. After crystallization firing, the complete absence of Zr^{4+}-bearing crystalline phases points to a scenario where the glass is Zr^{4+}-rich; the structure of the residual glass network, namely whether a $Zr^{4+} \leftrightarrow Si^{4+}$ substitution occurs or if Zr^{4+} remains in ionic form, is unclear [44]. Also, by increasing the Li_2O mol.% in relation to SiO_2, the range in which Li_2SiO_3 remains stable shows a tendency to surpass temperatures at which it would otherwise decompose in compositions having high SiO_2/Li_2O molar ratios [46].

During the crystallization firing the morphology of the Li_2SiO_3 crystals in *LMDpc* preserved some anisotropy in the CSD dimensions, but to a lower extent than in the pre-crystallization material. The lower relative growth took place in the *b* direction, while the dimension in the *c* direction increased by a factor of 17, resulting in a True CS of 35 nm. The crystal phase Li_3PO_4, primarily only detected in *pcLD*, grew from having CSD dimensions $b > a = c$ with a True CS of 7.4 ± 1.8 nm to $b > a > c$ and a True CS of 11.0 ± 0.7 nm after the crystallization firing. In *LMDpc*, Li_3PO_4 appeared in 10.7 wt.% in a different morphology than in *LDpc*, with CSD dimensions following $a > c > b$, but comparable True CS.

By comparing the crystallite sizes of Li_2SiO_3 (~35 nm) and $Li_2Si_2O_5$ (~230 nm) refined for *LMDpc*, with the dimensions of the crystalline structures observed in the SEM images (see Fig. 1), we can assume that both crystal phases occur as single crystals with the same dimensions as measured by XRD. It is not advisable to give any exact information about the CSDs of the $Li_2Si_2O_5$ phase for *LMDpc* and *LDpc* because they are too large to provide meaningful data by XRD measurements. Reduction of the CSD size generally results in peak broadening in the diffraction pattern. If crystallites are larger, the peak broadening resulting from crystallite size decrease does not

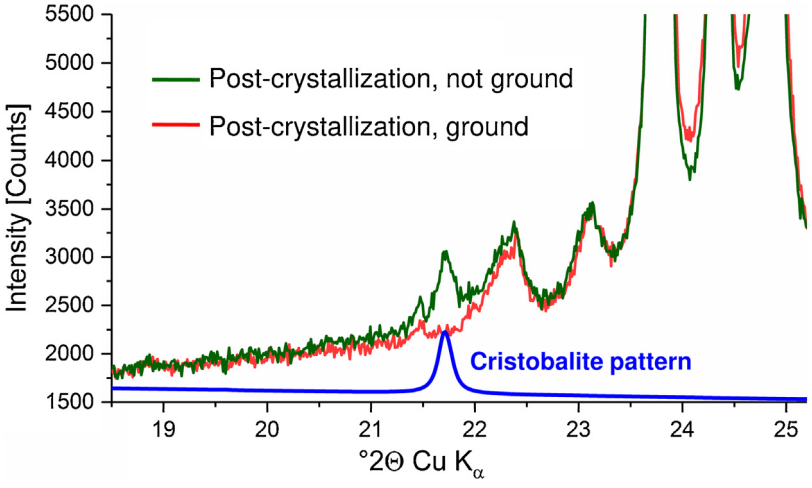

Fig. 5 – Diffraction patterns of LDpc before and after grinding; the reflection of cristobalite was calculated with software TOPAS.

Table 6 – Results of the mechanical testing for the material *LMD*: roughness parameter R_z, corrected Weibull modulus m_{corr}, the characteristic strength at 63.2% failure probability σ_0, and the characteristic critical crack size at failure at a 63.2% failure probability a_c.

	LMD					
	grinding pre-crystallized material	grinding + crystallization	crystallization + grinding	polishing + crystallization	crystallization + polishing	semi-elliptical crack + crystallization
R_z (μm) [S.D.]	7.72 [0.49]	3.91 [0.48]	6.19 [0.29]	0.5 [0.1]	0.5 [0.1]	–
m_{corr}[90% C.I.]	12.4 [9.7–15.8]	8.3 [6.5–10.6]	10.5 [8.2–13.4]	5.7 [4.5–7.3]	5.2 [3.9–6.4][a]	7.6 [4.8–12.3]
σ_0 (MPa) [90% C.I.]	109.03 [106.2–111.9]	443.84 [427.1–461.4]	188.29 [182.6–194.2]	514.09 [486.2–543.9]	537.03 [503.7–572.8][a]	598.7 [523.1–688.2]
a_c (μm) [90% C.I.]	17.74 [16.8–18.7]	2.48 [2.29–2.68]	13.83 [13.0–14.7]	1.84 [1.65–2.06] (*scratch*) 2.88 [2.58–3.2] (*natural*)	1.69 [1.49–1.92] (*scratch*) 2.64 [2.32–3.01] (*natural*)	1.37 [1.03–1.79] (*scratch*) 4.4 [3.4–5.8] (*semi-elliptical*)

[a] From Ref. [29].

Table 7 – Results of the mechanical testing for the material *LD*: roughness parameter R_z, corrected Weibull modulus m_{corr}, the characteristic strength at 63.2% failure probability σ_0, and the characteristic critical crack size at failure at a 63.2% failure probability a_c.

	LD					
	grinding pre-crystallized material	grinding + crystallization	crystallization + grinding	polishing + crystallization	crystallization + polishing	semi-elliptical crack + crystallization
R_z (μm) [S.D.]	4.50 [0.45]	4.58 [0.42]	8.42 [1.41]	0.5 [0.1]	0.5 [0.1]	–
m_{corr}[90% C.I.]	11.7 [9.2–14.9]	11.9 [9.3–15.2]	7.0 [5.5–9.0]	6.9 [5.4–8.8]	13.40 [10.0–16.30][a]	7.0 [4.5–11.1]
σ_0 (MPa) [90% C.I.]	190.86 [185.7–196.2]	550.66 [536.1–565.8]	246.67 [235.7–258.2]	762.84 [728.3–799.3]	609.8 [594.7–625.3][a]	669.5 [626.1– 717.6]
a_c (μm) [90% C.I.]	11.47 [10.8–12.1]	3.47 [3.29–3.66]	17.35 [15.8–19.0]	1.81 [1.50–1.98] (*scratch*) 2.81 [2.56–3.08] (*natural*)	2.83 [2.69–2.97] (*scratch*) 4.39 [4.18–4.62] (*natural*)	2.35 [2.04–2.68] (*scratch*) 7.6 [6.7–8.8] (*semi-elliptical*)

[a] From Ref. [29].

have any noticeably effect on the diffraction peak broadening any longer [47], and therefore no meaningful data for larger crystallite sizes can be obtained by the software TOPAS.

Once the available elements are consumed during the primary (performed by the manufacturer) and the secondary crystallizations, whether for primary crystal growth or phase transformations, the residual glasses may be depleted from, or enriched with certain elements. Additive oxides, not constituting crystalline phases, enrich the residual glass, such as Al^{3+}, K^{+}, Ce^{3+}, Zr^{4+}. The relative mass fractions of the oxides participating in crystal formation that remain in the glass, help to paint a picture of the crystallization kinetics too. In *LD* for example, the relative amount of SiO_2 in the residual glass increased after the first heat-treatment (to form the pre-crystallization material), to decrease after the crystallization firing; the opposite occurred for *LMD*. From the relative fraction of Li_2O in the residual glasses, it is clear that still 5.8 wt.% of Li_2O was "leftover" in *rgLMDpc*, while for *LD* all Li_2O was consumed for the formation of lithium-based crystal phases after the first heat treatment and crystallization firing. Hence, it is apparent that for *LMD* further crystallization of Li_2SiO_3 would be possible during the first heat-treatment if more time was given. Conversely, the relative amounts of Li_2O and P_2O_5 in *rgLD* point to a composition optimized to obtain the amount of crystalline fraction resulting in *LDpc*.

3.2. Surface effects

In the not-ground *LMDpc* samples (i.e. "surface"), the Li_3PO_4 could only be refined by application of March–Dollase correction for the preferred orientations in the (1 0 1) and the (1 1 0) planes, while the preferred orientation in (1 1 0) was extreme, with a March–Dollase factor ranging from 0.20 to 0.26, which indicates a very strong overrepresentation of the (1 1 0) plane in scattering direction. Since after grinding no preferred orientation was observed anymore, it can be concluded that the preferred orientation is indicative of a surface effect. While the Li_3PO_4 crystallites were statistically orientated in all directions in the Li_3PO_4 bulk sample, oriented precipitation of Li_3PO_4 was observed at the sample's surface. Despite of this observation, the quantities of Li_3PO_4 obtained at the surface and in the bulk sample were practically identical. Still, due to the extreme preferred orientation, the Li_3PO_4 quantities obtained at the surface are probably not very reliable. Furthermore, the results suggest that the CSD sizes of the Li_3PO_4 formed at the surface are higher than those obtained from the bulk sample, with CSD sizes of 21 ± 3 nm and 13 ± 1 nm, respectively. Indeed, the data obtained at the surface should also be treated with caution. Additionally, Y_2O_3 and Tb_2O_3 were detected in the not-ground sample, while the corresponding reflections disappeared in the ground ones (see Fig. 4). Hence, these oxides were also only precipitating at the surface. Another observation was that in the not-ground samples the quantity of $Li_2Si_2O_5$ was slightly increased, compared to the ground ones (i.e. "bulk"). Accordingly, slight decrease of the Li_2SiO_3 content was observed at the sample surface, but this was hardly significant.

In the *LDpc* samples, the main surface effect observed was the appearance of cristobalite on the sample's surface, which was not detected in the bulk sample (see Fig. 5).

Table 8 – Results of the fracture toughness B3B-K_{Ic} test for the *LMD* and *LD* materials in the pre- and post-crystallization states. Number of samples in parentheses.

	Pre-crystallization	Post-crystallization
LMD	0.913 ± 0.05 (9)	1.394 ± 0.10 (10)[a]
LD	1.285 ± 0.06 (10)	2.040 ± 0.10 (10)[a]

[a] From Ref. [32].

3.3. Mechanical properties and crack healing

Tables 6 and 7, summarize the results of the strength testing for the materials *LMD* and *LD*, respectively. Table 8 shows the results of the fracture toughness testing for both materials in the pre- and post-crystallization states. Through rearrangement of Eq. (6), the measured K_{Ic}-values allow us to obtain the characteristic size of the critical cracks responsible for failure in each strength testing condition:

$$a_c = \frac{1}{\pi}\left(\frac{K_{Ic}}{Y\sigma_{max}}\right)^2 \quad (8)$$

The geometric factor $Y = 1.1215$ is used under the assumption that the geometry of the defects created during grinding and polishing approximate that of surface scratches. It is of advantage that our K_{Ic}-values were obtained using the same test configuration (loading condition, specimen dimensions, short cracks) as in the strength tests, due to known loading and geometry effects [48]. Critical cracks induced by grinding were generally under 20 μm, relatively smaller than the semi-elliptical cracks produced for the B3B-K_{Ic} test ($a \sim 100$ μm, $2c \sim 260$ μm). Despite that, both cracks types are supposed to have become unstable at the same crack-tip stress intensity factor $K_{c,tip}$, since negligible *R*-curve behavior has been observed for *LMD* and *LD* in the post-crystallization state (i.e. $K_{c,tip} = K_{Ic}$) for cracks in that length scale [32,33]. In the pre-crystallization state, the fine Li_2SiO_3 microstructure is also not expected to have induced any significant *R*-curve, even though it certainly induced the toughening of the glass (the parent glass of *LD* was measured in Ref. [33] to $K_{Ic} = 0.75\,MPa\sqrt{m}$, which is within the range of other silicate glasses [49,50]). This is seen in Fig. 6, where the K_{Ic}-values measured here for both materials in either pre- and post-crystallization states were inserted into a plot of K_{Ic} as a function of crystallized volume fraction, reported in Ref. [51] for a stoichiometric lithium disilicate (LS_2, containing solely $Li_2Si_2O_5$ as crystalline phase). The data-point for *LDpc* seems to fit well in the trend for LS_2, just as *pcLD*, considering that it has mainly nanometric Li_2SiO_3 as reinforcing phase. The data-points for *LMD* seem to deviate away from the trendline towards lower K_{Ic}-values, not unexpectedly for *LMDpc* due to its finer microstructure; the K_{Ic}-value for *pcLMD* is rather low compared to *pcLD*, if this comparison is made based only in their crystallized vol.%.

In Ref. [29], multiple cracks in the bulk of *LMDpc* have been reported and speculated to be caused by a potential thermal incompatibility between the crystalline phase and a ZrO_2-enriched glass matrix. The same high-density cracking was also observed in this study for *pcLMD*, along with further hints to tensile residual stresses weakening the material: (i) *pcLMD*

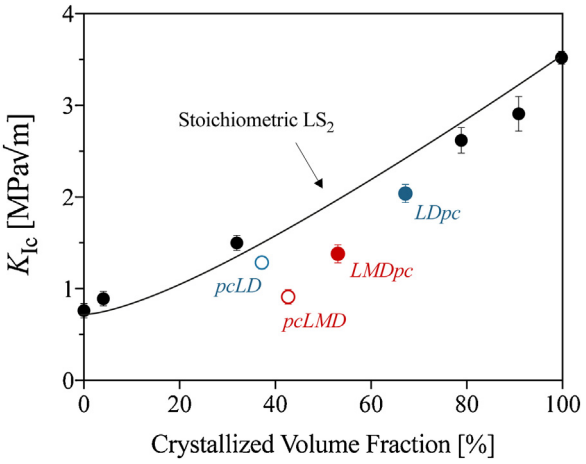

Fig. 6 – Plot of K_{Ic} vs. crystallized volume fraction [%] for a stoichiometric LS_2 from Ref. [51] obtained using double torsion specimens. The values for the pre- and post-crystallization samples of *LMD* and *LD* are inserted for comparison.

showed very deep lateral cracks from the Knoop indentations produced for B3B-K_{Ic} testing, usually spalling at the surface; (ii) lower indentation loads were needed for *pcLMD* and *LMDpc* to produce median cracks of comparable dimensions to those produced in *pcLD* and *LDpc*; (iii) the Knoop median crack formed in *pcLMD* showed concentric semi-elliptical markings resulting from multiple pop-in events during loading, similar to those observed in *LMDpc* in Refs. [8,32]. Presumably due to that, a much more pronounced damage resulted from the grinding of *pcLMD* compared to *pcLD*, with calculated critical crack sizes of 17.7 μm vs. 11.5 μm, respectively.

Our results show clearly that cracks generated in both pre-crystallized materials healed during the crystallization firing, demonstrated in strength and fracture toughness experiments. If that was not the case, the cracks generated during grinding of both materials in the partially-crystallized state would have preserved their dimensions, and the characteristic strength values in the second column of Tables 6 and 7 would have read 166.5 MPa and 303.1 MPa for *LMDpc* and *LDpc*, respectively, calculated by solving Eq. (6) for σ_{max}:

$$\sigma_{max} = \frac{K_{Ic,\,post-crystallization}}{Y\sqrt{\pi a_{c,\,pre-crystallization}}} \quad (9)$$

In that scenario, an increase in strength would result despite the preserved length of the unhealed cracks, simply because the post-crystallization materials have a higher value of K_{Ic}. However, the increase in strength was markedly higher in both instances, by 2.6 times for *LMDpc* and 1.8 times for *LDpc*, suggesting the condition $a_{c,\,post\text{-}crystallization} < a_{c,\,pre\text{-}crystallization}$ for both materials to be valid. The critical crack lengths for the ground pre-crystallized materials after the second-heat treatment were calculated to 2.5 μm and 3.5 μm, respectively. Apparently, healing of cracks in *LMD* seemed to have been slightly more efficient than in *LD*, if we consider only the change in crack length.

Another evidence of crack healing having taken place during the crystallization firing was observed during fracture of the B3B-K_{Ic} specimens that were indented in the pre-crystallization state and subsequently subjected to crystallization (far-right column in Tables 6 and 7). Valid B3B-K_{Ic} specimens should always fracture in two pieces if the long-axis of the crack is properly oriented towards one of the supporting balls, forming two fracture surfaces coinciding to the plane of the median crack. For both materials, these specimens fractured in multiple pieces (here the fracture origin is virtually impossible to detect using fractography), much like it occurs for strength specimens having small surface defects controlling failure. Not only that, the resulting characteristic strength from these B3B-K_{Ic} specimens were significantly higher than those for strength specimens that had been polished. The surface semi-elliptical pre-crack was therefore healed to an extent in which the stored elastic energy was high enough to induce multiple fracture surfaces, that is, the critical defect was very small. At this point, it begs the question whether the critical defect truly constituted a healed semi-elliptical pre-crack of decreased dimensions, or if the semi-elliptical pre-cracks healed entirely so that surface scratches from grinding (SiC paper of P600 grit were used to remove the Knoop damage zone and lateral cracks) started to control the fracture process.

In the lower-right cell of Tables 6 and 7, the size of the critical crack was calculated for both scenarios, i.e. for a "shrank" semi-elliptical crack with preserved *a/c* ratio by employing the geometric factor prescribed in Eq. (7), and for a surface scratch geometry. Against the latter scenario plays the fact that the critical crack size would amount to a shorter length than that calculated for the polished specimens. The high strength of these healed B3B-K_{Ic} specimens might therefore be tentatively explained by the lower geometric factor for the semi-elliptical crack in comparison to the more deleterious surface scratch. It is possible that the dimensional proportions of the semi-elliptical pre-crack change during healing, but this is fractographically very difficult to verify. Either way, the trend follows that of the strength experiments, namely, that healing was more effective for the *LMD* material than for *LD*.

Strength experiments conducted in specimens that were polished before the crystallization firing were meant to evaluate surface effects, as discussed in Section 3.2. Fine grinding followed by polishing of post-crystallization specimens is expected to have removed any surface layer subjected to microstructural changes, to expose the natural defect population in the bulk. No significant differences in this respect were seen for *LMDpc* between surface and bulk, despite the preferred orientation of Li_3PO_4, the slightly higher $Li_2Si_2O_5$ content and the presence of Y_2O_3 and Tb_2O_3 phases detected at the surface. In *LDpc*, the specimens in which the surface layer was maintained showed a noteworthy higher strength compared to polished specimens having the bulk material exposed. For this we can think of two probable explanations of mutually exclusive nature. The first considers the higher susceptibility of *LDpc* to grinding damage, evidenced by the strength and crack size values obtained from specimens that were coarse-ground after the crystallization firing. Materials with coarser microstructure have been shown to be more susceptible to material removal by grinding if crystal inter-

faces are weakened [52], as it is the case for lithium disilicate due to the anisotropic thermal mismatch between $Li_2Si_2O_5$ and the surrounding glass [33,53,54]. The strength attained by the specimens polished in the post-crystallization state might simply not represent the highest possible strength for the material, for the case where the polishing procedure did not manage to remove subsurface cracks completely. Defect sizes in the range of ~2.8 μm already approach the size of the microstructure, a typical limit for natural, not artificial defects [55]. In the case of the polishing procedure having produced identical surface conditions in both sets of specimens, that is, in specimens polished before or after final crystallization, the increase in strength for the former hints rather to a shielding of natural defects induced at the surface as result of the heat-treatment. The most obvious candidate is cristobalite as a fourth phase found in a 1 wt.% fraction in the not-ground specimens of *LDpc*. Cristobalite is known to form in similar compositions as *pgLD*, crystallizing first at 720 °C but completely dissolving at 820 °C [40,56]. In our samples, it is not clear if cristobalite was a reminiscence that dissolves at lower rates at the surface than in the bulk, or if it is a result of surface crystallization.

In pure silica glass, surface crystallization of cristobalite is known to induce cracking of the surrounding glass matrix thereby weakening the material, owed to the high volumetric shrinkage (~5 vol.%) of the β-cristobalite to α-cristobalite transformation at ~250 °C during cooling [57,58]. The opposite effect, that is, the strengthening of the material, would require the generation of compressive stresses by a crystal phase having a lower thermal expansion coefficient than that of the glass ($\alpha_{crystal} < \alpha_{glass}$). In this scenario, the calculated value for a_c in Table 7 for the samples polished before crystallization is underestimated, and amounts rather to the same value of a_c for the samples polished after crystallization. The shielding effect of the compressive residual stress can be estimated from the two experiments on polished samples. The crack tip is partly shielded by the compressive residual stress, now reading $K_{tip} = K_{appl} + |K_{sh}| = Y(\sigma_{appl} + |\sigma_{res}|)(\pi a_c)^{1/2}$. σ_{res} is estimated to be around −150 MPa regardless of the flaw type, simply the difference between the strength in the two experiments.

The existence of cristobalite also gives us room for speculating on the reduced crack healing capacity of *LD* compared to *LMD*. Assuming that cristobalite in *LD* really formed by surface crystallization during the crystallization firing, it is reasonable to presume that the same occurred on the surface of the cracks formed by indentation or grinding. Like particles in compacts, two opposing surfaces of a crack contact each other, especially at the crack tip. As the temperature increases above T_g, viscous flow is expected to fuse the two contacting surfaces together from the tip toward the "tail", but might be hindered by the concurrent process of surface crystallization. This is a known phenomenon in sintering of glass powders, used to deliberately control glass porosity. Thermal healing of cracks in glasses has been demonstrated by heating cracked glasses over T_g, a process suggested to be driven by viscous flow and capillariy forces [59], and to be influenced by the hydration state of the glass [60,61]. In non-isothermal sintering, the heating rate has been shown to be the foremost important factor in predisposing the glass to sinter or to crystallize [62,63]. Crystallization is rather fostered at lower heating rates [64]. In isothermal processes, the closer the temperature is to the *liquidus* temperature, the more sintering is favored over crystallization [64]. The crystallization firing of the two materials investigated here consisted of a non-isothermal section, in which *LD* was heated at 30 °C/min and *LMD* at 55 °C/min, and an isothermal part at comparable temperatures and times. The possible effect of the heating rate on the competition between crystallization and sintering of cracks in *LD* – and to which extent each process is more beneficial than the other – transcends the focus of this study and warrants further investigation.

4. Conclusions

We analyzed the parent glass composition of two commercial lithium silicate based glass-ceramics and identified significant differences in the amount of the main oxides. These were shown to affect the crystallization of Li_2SiO_3, $Li_2Si_2O_5$ and Li_3PO_4, resulting in different quantitative phase compositions after final crystallization. While one glass ceramic was shown to contain only $Li_2Si_2O_5$ and Li_3PO_4 after final crystallization, the second one additionally contained a high fraction of remaining Li_2SiO_3, which might be responsible for its lower mechanical performance. Defects introduced by grinding and indentation in the pre-crystallized materials have shown to heal during the crystallization firing, a desired effect bringing practical benefits to machined dental constructs. In one system, cristobalite crystallized only at the surface, and has been suggested to induce beneficial compressive stresses shielding surface cracks.

Acknowledgments

The materials utilized in this study were kindly donated by the manufacturers. The authors want to thank the Forschungsinstitut für Anorganische Werkstoffe – Glas/Keramik – GmbH (Hoehr-Grenzhausen) for conducting the XRF- and ICP-OES measurements of the bulk sample. This research project was partially financially supported by the Deutsche Forschungsgemeinschaft (DFG, German Research Foundation) — Grant Nr. HU 2498/1-1; GB 1/22-1.

REFERENCES

[1] Belli R, Petschelt A, Hofner B, Hajtó J, Scherrer SS, Lohbauer U. Fracture rates and lifetime estimations of CAD/CAM all-ceramic restorations. J Dent Res 2016;95:67–73.
[2] Curran P, Cattani-Lorente M, Wiskott HWA, Durual S, Scherrer SS. Grinding damage assessment for CAD-CAM restorative materials. Dent Mater 2017;33(3):294–308.
[3] Fraga S, Valandro LF, Bottino MA, May LG. Hard machining, glaze firing and hydrofluoric acid etching: do these procedures affect the flexural strength of a leucite glass-ceramic? Dent Mater 2015;31(7):E131–40.
[4] Quinn GD, Ives LK, Jahanmir S. Machining cracks in finished ceramics. Key Eng Mater 2005;290:1–13.
[5] Marshall DB, Lawn BR, Cook RF. Microstructural effects on grinding of alumina and glass-ceramics. J Am Ceram Soc 1987;70(6):C139–40.

[6] Chen S, Wei YJ, Chen MM, Zhang ZT. Bilateral treatment: a strategy for enhancing the mechanical strength of machinable veneers. Dent Mater 2010;26(10):961–7.
[7] Belli R, Scherrer SS, Lohbauer U. Report on fractures of trilayered all-ceramic fixed dental prostheses. Case Stud Eng Fail Anal 2016;7:71–9.
[8] Belli R, Wendler M, Zorzin JI, Lohbauer U. Practical and theoretical considerations on the fracture toughness testing of dental restorative materials. Dent Mater 2018;34(1): 97–119.
[9] Denry I. How and when does fabrication damage adversely affect the clinical performance of ceramic restorations? Dent Mater 2013;29(1):85–96.
[10] Ritzberger C, Schweiger M, Holand W. Principles of crystal phase formation in Ivoclar Vivadent glass-ceramics for dental restorations. J Non Cryst Solids 2016;432: 137–42.
[11] Belli R, Wendler M, de Ligny D, Cicconi MR, Petschelt A, Peterlik H, et al. Chairside CAD/CAM materials. Part 1: measurement of elastic constants and microstructural characterization. Dent Mater 2017;33(1):84–98.
[12] Hurle K, Belli R, Götz-Neunhoeffer F, Lohbauer U. Phase characterization during two-stage crystallization process of lithium silicate biomedical glass-ceramics. J Non Cryst Solids 2018;510:42–50. Accepted.
[13] Ectors D, Goetz-Neunhoeffer F, Neubauer J. A generalized geometric approach to anisotropic peak broadening due to domain morphology. J Appl Cryst 2015;48:189–94.
[14] Ectors D, Goetz-Neunhoeffer F, Neubauer J. Routine (an)isotropic crystallite size analysis in the double-Voigt approximation done right? Powder Diffr 2017;32:S27–34.
[15] Jansen D, Stabler C, Goetz-Neunhoeffer F, Dittrich S, Neubauer J. Does Ordinary Portland Cement contain amorphous phase? A quantitative study using an external standard method. Powder Diffr 2011;26(1):31–8.
[16] Ectors D. Advances in the analysis of cementitious reactions and hydrate phases, Friedrich-Alexander-Universität Erlangen-Nürnberg, Dissertation; 2016.
[17] Hesse KF. Refinement of the crystal structure of lithium polysilicate. Acta Cryst 1977;B33:901–2.
[18] De Jong BHWS, Super HTJ, Spek AL, Veldman N, Nachtegaal G, Fischer JC. Mixed alkali systems: structure and Si-29 MASNMR of Li2Si2O5 and K2Si2O5. Acta Cryst. B 1998;54:568–77.
[19] Zemann J. Die Kristallstruktur Von Lithiumphosphat, Li3PO4. Acta Crystallogr 1960;13:863–7.
[20] Lehmann MS, Christensen AN, Fjellvag H, Feidenhansl R, Nielsen M. Structure determination by use of pattern decomposition and the rietveld method on synchrotron X-ray and neutron powder data — the structures of Al2y4o9 and I2o4. J Appl Cryst 1987;20:123–9.
[21] Smrock L, Duris P. Rietveld refinement of Y2O3 — comparison of two profile functions. In: Hasek J, editor. X-ray and neutron structure analysis in materials science. Boston, MA: Springer; 1989.
[22] Zachariasen WH. Skifter utgitt av Det Norske Videnskap-akademi i Oslo, 1: matematisk-Naturvidenskapelig; 1928. p. 1–165 (Untersuchung über die Kristallstruktur von Sesquioxydn und Verbindungen ABO3).
[23] Downs RT, Palmer DC. The pressure behavior of alpha-cristobalite. Am Mineral 1994;79(1–2):9–14.
[24] Jansen D, Goetz-Neunhoeffer F, Lothenbach B, Neubauer J. The early hydration of Ordinary Portland Cement (OPC): an approach comparing measured heat flow with calculated heat flow from QXRD. Cem Concr Res 2012;42(1):134–8.
[25] Prince E. International union for crystallography, international tables for crystallography, volume C: mathematical physical and chemical tables. 3rd ed. Dordrecht: Kluwer Academic Publishers; 2004.
[26] Chen K. Increasing the reliability of dental prosthesis by understanding crack initiation during crystallization of lithium silicate glass-ceramics, Dissertation Friedrich-Alexander-Universität Erlangen-Nürnberg; 2017.
[27] Börger A, Supancic P, Danzer R. The ball on three balls test for strength testing of brittle discs: stress distribution in the disc. J Eur Ceram Soc 2002;22(9–10):1425–36.
[28] Börger A, Supancic P, Danzer R. The ball on three balls test for strength testing of brittle discs: part II: analysis of possible errors in the strength determination. J Eur Ceram Soc 2004;24(10–11):2917–28.
[29] Wendler M, Belli R, Petschelt A, Mevec D, Harrer W, Lube T, et al. Chairside CAD/CAM materials. Part 2: flexural strength testing. Dent Mater 2017;33(1):99–109.
[30] Danzer R, Supancic P, Harrer W. Biaxial tensile strength test for brittle rectangular plates. J Ceram Soc Jpn 2006;114(1335):1054–60.
[31] Harrer W, Danzer R, Supancic P, Lube T. The ball on three balls test: strength testing of specimens of different sizes and geometries. In: Proceedings of the 10th International Conference of the European Ceramic Society (ECerS); 2007. p. 1271–5.
[32] Belli R, Wendler M, Petschelt A, Lube T, Lohbauer U. Fracture toughness testing of biomedical ceramic-based materials using beams, plates and discs. J Eur Ceram Soc 2018;38(16):5533–44.
[33] Belli R, Wendler M, Cicconi MR, de Ligny D, Petschelt A, Werbach K, et al. Fracture anisotropy in texturized lithium disilicate glass-ceramics. J Non Cryst Solids 2018;481:457–69.
[34] ASTM C1421. Standard test methods for determination of fracture toughness of advances ceramics at ambient temperature. ASTM International; 2010.
[35] Lube T, Rasche S, Nindhia TGT. A fracture toughness test using the ball-on-three-balls test. J Am Ceram Soc 2016;99(1):249–56.
[36] Strobl S, Rasche S, Krautgasser S, Sharova E, Lube T. Fracture toughness testing of small ceramic discs and plates. J Eur Ceram Soc 2014;34:1637–42.
[37] Strobl S, Supancic P, Lube T, Danzer R. Surface crack in tension or in bending — a reassessment of the Newman and Raju formula in respect to fracture toughness measurements in brittle materials. J Eur Ceram Soc 2012;32:1491–501.
[38] Strobl S, Supancic P, Lube T, Danzer R. Corrigendum to “Surface crack in tension or in bending — a reassessment of the Newman and Raju formula in respect to fracture toughness measurements in brittle materials (vol 32, pg 1491, 2012)”. J Eur Ceram Soc 2018;38(1):355–8.
[39] Newman JC, Raju IS. An empirical stress-intensity factor equation for the surface crack. Eng Fract Mech 1981;15(1–2):185–92.
[40] Holand W, Apel E, van’ t Hoen C, Rheinberger V. Studies of crystal phase formations in high-strength lithium disilicate glass-ceramics. J Non Cryst Solids 2006;352(38–39):4041–50.
[41] Bischoff C, Eckert H, Apel E, Rheinberger VM, Holand W. Phase evolution in lithium disilicate glass-ceramics based on non-stoichiometric compositions of a multi-component system: structural studies by Si-29 single and double resonance solid state NMR. Phys Chem Chem Phys 2011;13(10):4540–51.
[42] Huang S, Cao P, Li Y, Huang Z, Gao W. Nucleation and crystallization kinetics of a multicomponent lithium disilicate glass by in situ and real-time synchrotron X-ray diffraction. Cryst Growth Des 2013;13:4031–8.
[43] Höland W, Beall GH. Glass-ceramic technology. 2nd ed. Hoboken, New Jersey: Wiley; 2012. p. 86.

[44] Kruger S, Deubener J, Ritzberger C, Holand W. Nucleation kinetics of lithium metasilicate in ZrO2-bearing lithium disilicate glasses for dental application. Int J Appl Glass Sci 2013;4(1):9–19.
[45] Apel E, van't Hoen C, Rheinberger V, Holand W. Influence of ZrO_2 on the crystallization and properties of lithium disilicate glass-ceramics derived from a multi-component system. J Eur Ceram Soc 2007;27(2–3):1571–7.
[46] Gaddam A, Fernandes HR, Tulyaganov DU, Ribeiro MJ, Ferreira JMF. The roles of P2O5 and SiO2/Li2O ratio on the network structure and crystallization kinetics of non-stoichiometric lithium disilicate based glasses. J Non Cryst Solids 2018;481:512–21.
[47] Jenkins R, Snyder RL. Introduction to X-ray powder diffractometry. New York: John Wiley & Sons Inc.; 1996. p. 89–90.
[48] Fett T. New contributions to R-curves and bridging stresses — applications of weight functions. Karlsruhe: KIT Scientific Publishing; 2012.
[49] Quinn GD, Swab JJ. Fracture toughness of glasses as measured by the SCF and SEPB methods. J Eur Ceram Soc 2017;37:4243–57.
[50] Quinn GD, Swab JJ, Patel P. Fracture toughness of modern and ancient glasses and glass ceramics as measured by the SEPB method. Ceram Eng Sci Proc 2018;39:3–13.
[51] Serbena FC, Mathias I, Foester CE, Zanotto ED. Crystallization toughening of a model glass-ceramic. Acta Mater 2015;86:216–28.
[52] Xu HHKX, Jahanmir S. Scratching and grinding of a machinable glass-ceramic with weak interfaces and rising T-curve. J Am Ceram Soc 1995;78(2):497–500.
[53] Pinto H, Ito L, Crovace M, Ferreira EB, Fauth F, Wroblewski T, et al. Surface and bulk residual stresses in Li2O-2SiO2 glass-ceramics. J Non Cryst Solids 2007;353:2307–17.
[54] Mastelaro VR, Zanotto ED. Anisotropic residual stresses in partially crystallized Li_2O-$2SiO_2$ glass-ceramics. J Non Cryst Solids 1999;247:79–86.
[55] Danzer R, Lube T, Supancic P, Damani R. Fracture of ceramics. Adv Eng Mater 2008;10(4):275–98.
[56] Lien W, Roberts HW, Platt JA, Vandewalle KS, Hill TJ, Chu T-MG. Microstructural evolution and physical behavior of a lithium disilicate glass-ceramic. Dent Mater 2015;31:928–40.
[57] Breneman RC, Halloran JW. Stress development and fracture of surface nucleated cristobalite on silica glass. J Am Ceram Soc 2014;97(11):3483–8.
[58] Breneman RC, Halloran JW. Effect of cristobalite on the strength of sintered fused silica above and below the cristobalite transformation. J Am Ceram Soc 2015;98(5):1611–7.
[59] Hrma P, Han WT, Cooper AR. Thermal healing of cracks in glass. J Non Cryst Solids 1988;102(1–3):88–94.
[60] Girard R, Faivre A, Despetisz F. Influence of water on crack self-healing in soda-lime silicate glass. J Am Ceram Soc 2011;94(8):2402–7.
[61] Girard R, Faivre A, Despetis F. Crack healing by thermal treatment in float glass: the effect of tin. J Am Ceram Soc 2014;97(11):3463–8.
[62] Prado MO, Fredericci C, Zanotto ED. Glass sintering with concurrent crystallisation. Part 2. Nonisothermal sintering of jagged polydispersed particles. Phys Chem Glasses: Eur J Glass Sci Technol B 2002;43(5):215–23.
[63] Prado MO, Fredericci C, Zanotto ED. Non-isothermal sintering with concurrent crystallization of polydispersed soda-lime-silica glass beads. J Non Cryst Solids 2003;331(1–3):157–67.
[64] Prado MO, Nascimento MLF, Zanotto ED. On the sinterability of crystallizing glass powders. J Non Cryst Solids 2008;354(40–41):4589–97.